crystals

MDPI

Article

Synthesis, Cytotoxic Activity, Crystal Structure, DFT, Molecular Docking Study of β-Enaminonitrile Incorporating 1*H*-Benzo[*f*]Chromene Moiety

Mosa H. Alsehli [1], Lali M. Al-Harbi [2], Rawda M. Okasha [3], Ahmed M. Fouda [4], Hazem A. Ghabbour [5], Abd El-Galil E. Amr [6], Ahmed A. Elhenawy [7,8,*] and Ahmed M. El-Agrody [7,*]

1 Department of Chemistry, College of Science, Taibah University, Al Medina Al Munawwara 30002, Saudi Arabia
2 Chemistry Department, Faculty of Science, King Abdul-Aziz University, Jeddah 21589, Saudi Arabia
3 Chemistry Department, College of Science, Taibah University, Medina 30002, Saudi Arabia
4 Chemistry Department, Faculty of Science, King Khalid University, Abha 61413, Saudi Arabia
5 Department of Medicinal Chemistry, Faculty of Pharmacy, University of Mansoura, Mansoura 35516, Egypt
6 Applied Organic Chemistry Department, National Research Center, Dokki, Giza 12622, Egypt
7 Chemistry Department, Faculty of Science, Al-Azhar University, Nasr City, Cairo 11884, Egypt
8 Chemistry Department, Faculty of Science and Art, Albaha University, Mukhwah, Albaha 65731, Saudi Arabia
* Correspondence: elhenawy_sci@hotmail.com (A.A.E.); elagrody_am@azhar.edu.eg (A.M.E.-A.)

Abstract: In this work, we used microwave irradiation conditions to synthesize β-enaminonitrile (**4**), which was affirmed using single crystal X-ray diffraction and the different spectral data. Two tumor cell lines, MCF-7 and MCF-7/ADR, as well as two normal cell lines, HFL-1 and WI-38, were used to assess the anticancer activity of compound **4**. The studied molecule exhibited potent efficacy against the MCF-7 and MCF-7/ADR cell lines compared with the reference drugs. Furthermore, target compound **4** had feeble activity against HFL-1 and WI-38. The chemical reactivity was discussed using DFT and QTAIM analysis to study the intrinsic electronic properties of compound **4**. A molecular docking study was also conducted to examine their binding affinity to the EGFR. Compound **4** revealed a stable binding mode at the enzyme active pocket more than the reference inhibitor. The docking analysis was performed for molecule (**4**).

Keywords: β-enaminonitrile; microwave irradiation; X-ray; antitumor activity; docking study

Citation: Alsehli, M.H.; Al-Harbi, L.M.; Okasha, R.M.; Fouda, A.M.; Ghabbour, H.A.; Amr, A.E.-G.E.; Elhenawy, A.A.; El-Agrody, A.M. Synthesis, Cytotoxic Activity, Crystal Structure, DFT, Molecular Docking Study of β-Enaminonitrile Incorporating 1*H*-Benzo[*f*]Chromene Moiety. *Crystals* **2023**, *13*, 24. https://doi.org/10.3390/cryst13010024

Academic Editor: Sławomir Grabowski

Received: 9 November 2022
Revised: 5 December 2022
Accepted: 13 December 2022
Published: 23 December 2022

1. Introduction

Chromenes and benzochromenes are one of the superior biological active families that have been the central unit in several natural and synthetic pharmacological agents [1]. According to their biomedical characteristics, these materials have been assimilated into numerous applications such as antibacterial and antifungal activity [2–4], cytotoxic activity [5], and vascular disrupting agents [6]. Additionally, 4*H*-benzo[*h*]chromene scaffolds have been stated to target signaling pathways important for cancer cell proliferation and anticancer drug development. For example, 2-amino-4-aryl-4*H*-benzo[*h*]chromene-3-carbonitrile and 6-chloro/methoxy derivatives act as active antitumor agents [7], 6-methoxy derivative of 2-amino-4-aryl-4*H*-benzo[*h*]chromene-3-carbonitrile has also been engaged in targeting *c*-Src kinase enzyme [8], caspase3/7, apoptotic-effects, induced cell-cycle-analysis, and the inhibition of the topoisomerase-enzyme [9], 2-acetylamino/ethoxymethyleneamino derivative of 6-methoxy-4*H*-benzo[*h*]chromene-3-carbonitrile induced cell cycle arrest prompting apoptosis [8,9], and halogenated 4*H*-benzo[*h*]chromene, producing powerful anticancer analogues that target the *c*-Src kinase enzyme [10], respectively.

Furthermore, 1*H*-benzo[*f*]chromene is a privileged scaffold as well as one of the most promising classes of oxygen-heterocyclic systems with a variety of biological activity pro-

files. 8-Bromo/methoxy derivatives of 1*H*-benzo[*f*]chromene-2-carbonitriles inhibit c-Src kinase and proliferation, induce cell cycle arrest at the G2/M, S, and S-G2/M phases, increase the production of caspases 3/8/9, induce apoptosis in human cancer cells via dual inhibition of topoisomerase I/II, and trigger apoptosis in preestablished breast cancer xenografts grown on chick chorioallantoic membranes while exhibiting low systemic toxicity [11]. Additionally, 9-bromo/methoxy derivatives of 1*H*-benzo[*f*]chromene-2-car-bonitriles induce cell cycle arrest at the G2/M, S, and S-G2/M phases, increase the production of caspases 3/7/9, and finally cause intrinsic and extrinsic apoptotic cell death [12,13]. Additionally, they have been utilized as powerful molecules that have apoptotic impacts with DNA binding attributes via an assortment of cell types [14]. Furthermore, the chromene scaffold has an inhibition characteristic of human acetylcholinesterase, where the prospect of treating Alzheimer's disease (AD) is achievable [15]. Among the synthetic strategies of chromene compounds, microwave irradiation has been the most prosperous procedure for immediate, sustainable productivity of the desired molecules [16]. Recently, computer-aided approaches including molecular docking [16], ADMET assessment, and DFT calculations [17] have been applied in several fields such as drug discovery and drug design.

The development of the demanded molecule in a crystalline form provides precise structural identification and absolute configuration, which contributes to our understanding of the implementation of new drug candidates.

The rational design of the 8-methoxy-1*H*-benzo[*f*]chromene derivatives (**4**) was concerned with the 1*H*-benzo[*f*]chromene scaffold itself, the type of substituent at the 8-postion, and on the aryl group at the 1-postion, which appears to play a crucial role in the cytotoxic activity, and a comparison of the behaviors of the synthesized derivatives linked to a 8-methoxy group at the 8-position with the previously synthesized derivatives with a bromine at the 8-position [7]. The comparison showed that the target derivative **4** exhibited a significant impact on their activities against cancer cell lines that were more potent than or similar to the previously synthesized derivatives [7].

In the continuation of our effort toward conceiving potent oxygen-heterocyclic-based antiproliferative agents, this report outlines the synthesis of 3-amino-1-(4-bromophenyl)-8-methoxy-1*H*-benzo[*f*]chromene-2-carbonitrile, and explores its crystallographic structure, antitumor capability against cancer cell lines (MCF-7, MCF-7/ADR) and two normal (HFL-1 and WI-38) cell lines, which was confirmed through molecular docking assessment.

2. Experimental Section

2.1. Materials and Equipment

All chemicals were purchased as mentioned in the Supplementary Materials.

*2.2. Synthesis of 3-Amino-1-(4-Bromophenyl)-8-Methoxy-1H-Benzo[f]chromene-2-Carbonitrile (**4**)*

Compound **4** was prepared as previously reported [7].

2.3. X-Ray Crystallography Analysis

The single crystal for compound **4** was obtained by the slow evaporation from ethanol at room temperature and then used Bruker SAINT. SHELXT [18,19]; the other procedures are illustrated in the Supplementary Materials.

2.4. Biological Screening

In vitro screening for the examined compound **4** was performed using the MTT colorimetric assay, as described in the Supplementary Materials.

2.5. Hirschfeld Fingerprint Analysis

The 2D and 3D Hirschfeld were extracted from Crystal-Explorer, as described in the Supplementary Materials.

2.6. Quantum Simulations

DFT with B3LYP using the 6-311**G(d,p) basis set was used for all computations and optimization geometry using Maestro Elements 12.5 [20–23]. The Van der Waals surface was estimated for the MEP-surface through the 0.001 a.u. isosurface. "QTAIM, Bader's quantum theory of 'atoms-in-molecules" in combination with the noncovalent interaction plot were plotted using the Multiwave Function package [21].

2.7. Molecular Docking with Their Validation Method

The 3D EGFR proteins were handled using the Glide-tool, which uses a rigid receptor docking, as mentioned in [20]. The error correction for the structure of the catalytic EGFR site was performed by supplementing the hydrogen and partial charges using Amber12: EHT, then minimized through utilizing the same force field with RMSD = 0.100. The catalytic site was identified and analyzed using Site Finder, which was implemented in the Schrodinger program [20], which is based on alpha spheres as well as energy model. Water and inhibitor molecules were eliminated, and then H-atoms were supplemented to the obtained crystal structure, then charged by assigning them with the same force field. The original inhibitor was removed from the active site, then the synthesized ligand and reference inhibitor redocked into this empty active site. At the centroid of the predicted binding site or active site, a grid cube of defined size is generated in the center of the binding site, which accounts for the receptor grid generation. A cubic-box was applied on the centroid-binding pocket to generate the receptor. The size of the box was assigned to 12 Å × 12 Å × 12 Å for docking. Then, the other molecular docking with procedures was applied according to using the original precision (SP) scoring function of the glide scoring function (using induced-fit algorithm), which was generated to measure the binding affinity. The different poses of ligands were generated. Finally, assigned poses were assigned a score based on the free energy in kcal/mol. The most potent pose was selected based on the lowest free energy and RMSD [24–26].

2.8. Molecular Dynamic Simulations

Molecular dynamics simulation of the protein–ligand complexes was performed using GROMACS 2021 and the Linux 5.4 package. The GROMOS96 forcefield was selected as the force field for proteins and the ligand topologies were generated from the PRODRG server. All of the complexes were solvated using simple point charge (SPC) water molecules in a rectangular box. To make the simulation system electrically neutral, the required number of Na+ and Cl− ions were added while 0.15 mol/L salt concentrations were set in all of the systems. Using the steepest descent method, all of the solvated systems were subjected to energy minimization for 5000 steps. Afterward, the NVT (constant number of particles, volume, and temperature) series, NPT (constant number of particles, pressure, and temperature) series, and the production run were conducted in the MD simulation. The NVT and the NPT series were conducted at a 300 K temperature and 1 atm pressure for the duration of 300 ps. AA V-rescale thermostat and Parrinello–Rahman barostat were selected for the performed simulation. Finally, the production run was performed at 300 K for a duration of 150 ns (nanoseconds) [26–28].

3. Results and Discussion

3.1. Chemistry

The synthetic pathway employed to synthesize compound **4** is depicted in Scheme 1, as previously reported [7]. In a one-pot three component heterocyclocondensation methodology, 3-amino-1-(4-bromophenyl)-8-methoxy-1*H*-benzo[*f*]chromene-2-carbonitrile (**4**) was acquired via the interaction of 6-methoxynaphthalen-2-ol (**1**) with 4-bromobenzaldehyde (**2**) and malononitrile (**3**) in a basic ethanolic solution. The reaction was triggered with the microwave irradiation conditions. The optimum condition was resolved for this reaction, which was found at 400 W irradiation for 2 min at 140 °C and the reaction monitored via TLC. Because compound **4** has a chiral property, the stereochemistry for the 1-position of

the 1*H*-benzo[*f*]chromene moiety was determined by measuring its specific rotation using a Carl Zeiss polarimeter. According to our findings, compound **4** exhibits zero rotation (i.e., optically inactive) and is obtained in the form of a racemic (±) mixture [8], Scheme 1. In addition, the structure and purity of compound **4** were confirmed by the spectral data (see Supplementary Materials, Figures S1–S3) and the X-ray single crystal analysis.

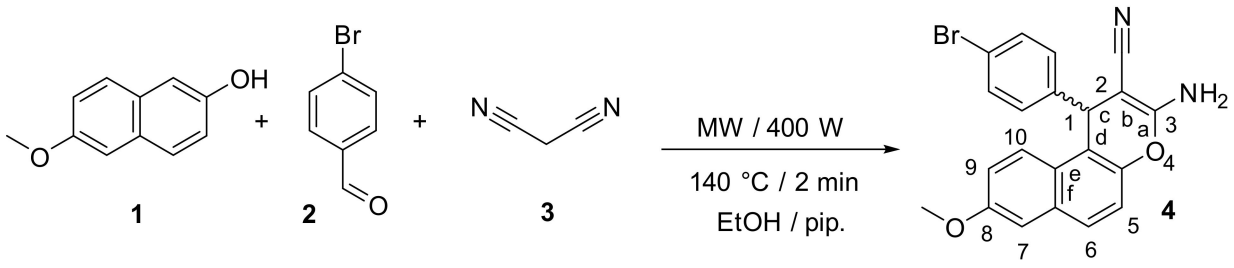

Scheme 1. Synthesis of 3-amino-1-(4-bromophenyl)-8-methoxy-1*H*-benzo[*f*]chromene-2-carbonitrile (**4**).

3.2. Crystal Data

The crystallographic data for the addressed compounds, $C_{21}H_{15}BrN_2O_2$, are listed in Table S1. According to Figure 1, the compound **4** asymmetric units each contain one molecule. The bond lengths and angles were all within the expected ranges [29]. The crystal packing for molecule **4** was connected by two intermolecular H-bonds (Table 1).

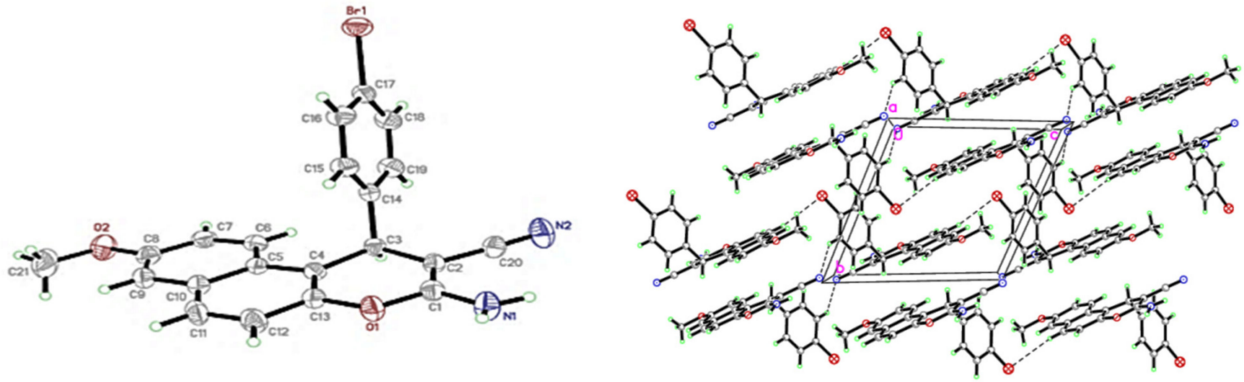

(**a**) (**b**)

Figure 1. (**a**) XRD for **4** which was plotted using ORTEP, non-H atoms, represented by ellipsoids (50% probability level). (**b**) Three-dimensional networks for molecular packing. H-bonds are represented in dashed lines.

Table 1. The geometry for the H-bond (Å, °) for compound **4**.

D—H•••A	D—H	H•••A	D•••A	D—H•••A
N1—H2N1···N2i	0.85 (4)	2.19 (4)	3.033 (4)	172 (4)
C18—H18A···N2ii	0.9300	2.5100	3.306 (5)	143.00
Symmetry codes: (i) −x, −y + 2, −z; (ii) −x + 1, −y + 2, −z.				

Compound **4** was crystallized in the triclinic system and the P1 (2) space group with unit cell parameters of **a** = 8.9866(3)Å, **b** = 10.8369(4)Å, and **c** = 11.2286(4)Å, α = 103.576 (2)°, β108.816(2)°, γ110.455(2)°. The unit cell volume was 892.292 (6) Å^3 (Supplementary Materials Table S1). Molecule **4** comprised three fused rings, which were in perfect planarity mode, as illustrated in Figure 1. The benzo[*f*]chromene ring occurred in the envelope style and linked in a perpendicular mode with 4-bromophenyl.

The OCH_3, CN, and NH_2 groups were located out of the plane for the three rings. These groups twisted from the main core by 117° (C21-O2-C8), 119° (C2-C20-N2), and 110° (C1-C2-N2). Furthermore, the OCH_3, CN, and NH_2 groups showed a plane deviation by 179.21°, 41.60°, and 166.63° from the main plane (through the three fused rings), indicating that it is perpendicular to the benzo[*f*]chromene ring, as shown in Supplementary Materials Table S2.

Structural Dimers of Crystal Packing

Crystal Explorer [30] was applied to extract the molecular dimer for compound **4** by calculating the intermolecular interaction energies. The result showed that there were four structural motifs (Dimers **1–4**). The interaction geometries with the corresponding energies are shown for dimers **1–4** (Table 2). The dimer structure for compound **4** showed that the intermolecular interaction energy ranged from −73.7 to −9.9 kJ/mol^{-1} (Table 2). The intermolecular forces stabilized these **1–4** dimers including C–H···N, C–H●●●O, CH●●●Br, π●●●π, respectively (Figure 2). Etot (kJ/mol^{-1}) for the four dimers included dimer 1 = −4–73.7, dimer 2 = −61, dimer 3 = −39.4, and dimer 4 = −28.9 (Figure 2).

Table 2. The interaction energies (kJ/mol^{-1}) at B3LYP/6-31**G(d,p) of the intermolecular interactions.

Dimer	Symmetry	R	E_{ele}	E_{pol}	E_{dis}	E_{rep}	E_{tot}
1	−x, −y, −z	6.89	−19.9	−2.8	−93.7	50.1	−73.7
2	−x, −y, −z	11.55	−70.8	−17.6	−13.2	62.3	−61
3	−x, −y, −z	6.28	−20	−2.8	−47	40	−39.4
4	−x, −y, −z	8.87	−3.8	−1.9	−33.9	9.7	−28.9

R: centroid-to-centroid distance (Å) of the molecular pair (main atomic position).

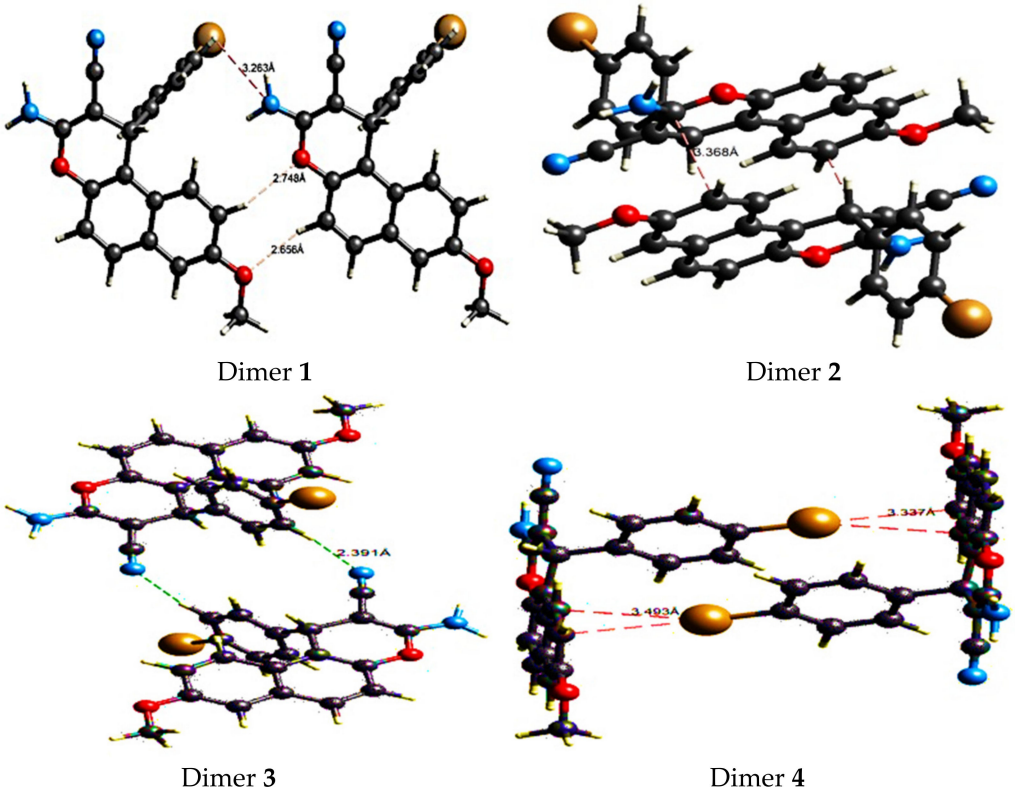

Figure 2. Molecular dimers **1–4** and the intermolecular contacts are shown as dashed lines and distances in Å.

The feeble intramolecular interactions including C17—H17, H2N1●●●N2, and H18N1●●●N2 were responsible in the stabilization of the structure of compound **4**. These interactions serve to determine the rotation of the OCH_3, CN, and NH_2 fragments as well as formulate the ribbon form along the b-axis, which is necessary to connect into a stepped pattern approximately parallel to each other, as shown in Figure 2.

3.3. Profile for the Crystal-Packing

The intermolecular bonds and Hirschfeld "HF" surfaces that contribute to the molecular packing of compound **4** (Figure 3). "dnorm" was calculated as reported in [31]. The "rvdWi" and "rvdWe" were connected to Van der Waals-radii for the nearest interior with exterior particles via the morphology. The +ve value of dnorm related to short rvdW, but the lengthy rvdW had a −ve value. Crystal-Explorer [30] was used to find (de and di) the correlation for the HF, and the 3D HF is shown in Figure 3, over; dnorm in (−0.4643–1.5692) Å, di (0.8260 to 2.7645) Å, de (0.8253 to 2.6546), shape index (−1.00 to 1.00) Å, curvedness (−4.00 to 4.00) Å, and fragment-patch (0.00–13.00) Å, respectively. The shortest interactions that contributed in packing molecule **4** included "Br●●●O/Br●●●O,O●●●C/O●●●C&N●●●C/N●●●C". The "O●●●H" interactions were characterized by the red zone in the dnorm-fingerprint; these connections are smaller than the vdWs radii, as represented in Figure 3.

In addition, relatively long C●●●C (4.7%) and Br●●●H/Br●●●H (9.5%) contacts were also shared with the crystal packing. The most predominant was H●●●H with 36.1% in the whole map area. Furthermore, the *crv* fingerprint was used to examine the shape of the surface of the particles. The sites with the flat-surface exhibited the least amount of curvature, but the zones that had a sharp curvature were relevant to the degree of sharp curvedness. Due to the interactions between nearest particles, the surface was split into two patches. Si is a sensitive indicator via any variation in the lattice shape. The red triangles are used to show the concave-zone, which is localized on a particle's upper plane and indicates that bromophenyl is restricted outside of the surface. The data, which were concluded from SI, were obeyed with 2D-fingerprint. The absence of blue and red triangles located in SI and the increase in the green-flat zone in Crv showed a lack of significant π–π stacking interactions.

3.4. Weak Interaction Profile

The "RDG, reduced-density-gradient" for "NCI, non-covalent interactions" is a powerful technique to identify the weak connection between molecules. NCI plays a crucial role, which is responsible in the 3D-arrangement of protein and nucleic acids. Furthermore, the crystallinity, material design, medicinal design, and self-assembly are all significantly impacted by NCI. The weak inter and intramolecular interactions were investigated by (RDG) scatter graph, which is a colorful relationship between RDG via sign (λ2), which offers a restricted range for weak interaction types, and is calculated as previously reported [32]. The restricted (negative to positive) range refers to the attractive, repulsive, and moderate types of interaction [32]. The NCI graph for compound **4** is displayed in Figure 4. The negative energy value (−0.02 a.u.) showed the presence of Van der Waal interactions. In this case, a strong-repulsive-force was noticed, which is related to steric-force, and centered in the range (0.01−0.048 a.u.), and there were also values showing weak H-interactions in the monomer of compound **4**. In addition, RDG was directly proportional to the particle's electronic cloud and introduced as an isosurface (Figure 4). The maximum RDG-electronic-density was depicted in a green-color (0.0.02 to 0.800) that localized over the O atom of the OCH_3 group and O atom of the pyran fragments for compound **4**.

The LOL "localized orbit locator" was applied to analyze the relation between the electrical and geometric structure to enhance the understanding of the bond mechanics of the molecule. The topological features of the molecule **4** monomer in the aqueous phase were studied using LOL analyses. In Figure 4, the green color denotes a location with large LOL values (localization area), while blue and gray represent a region with poor LOL

values (delocalization area) for the monomer [33]. These graphs show blue and gray areas localized around the H atoms of the rings due to the electron depletion. The green and blue zones (rich electron sites) were capped over the carbon atoms, corresponding to the H-bond donor in monomers to produce the dimer.

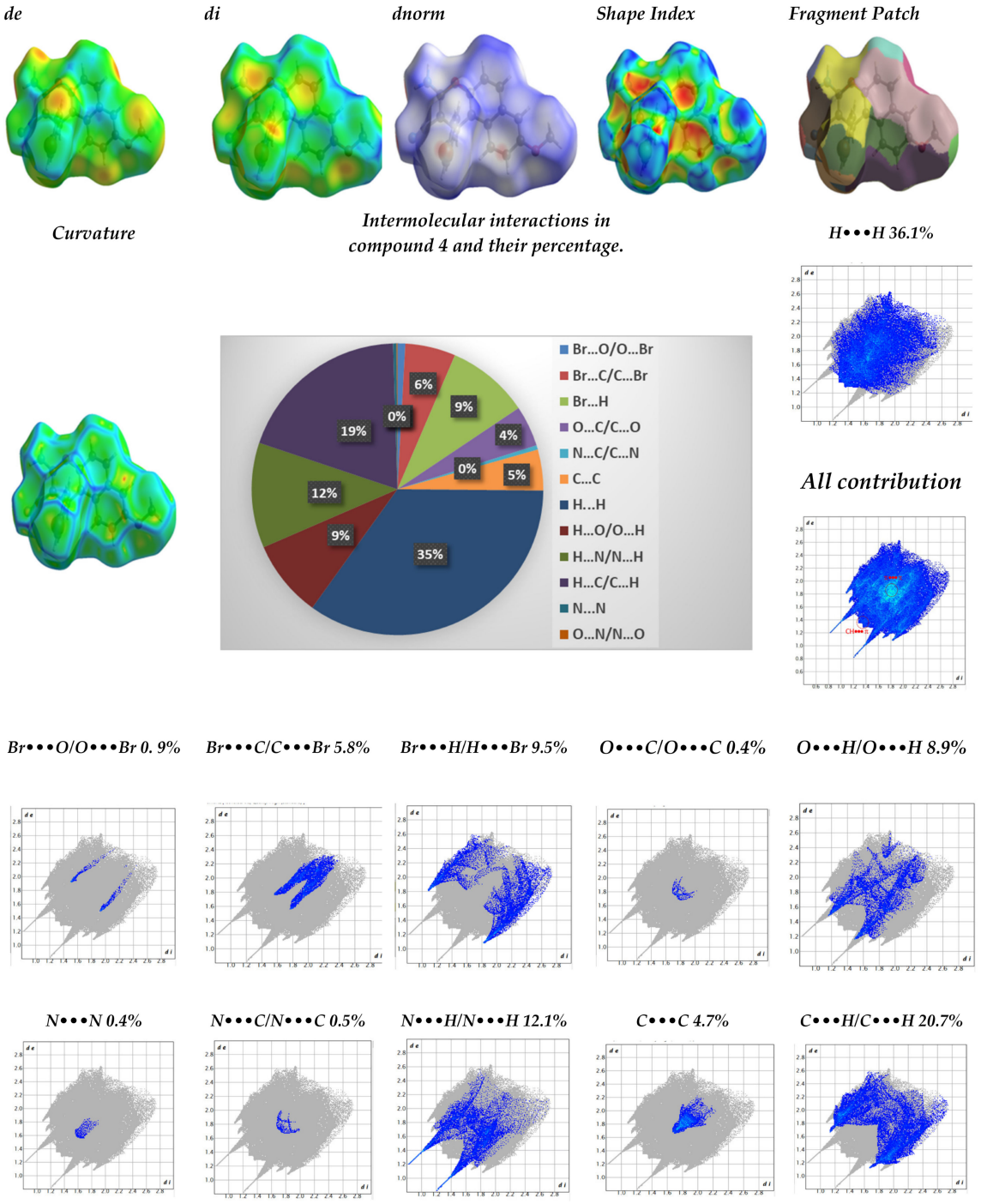

Figure 3. The "HF" Hirschfeld, 2D interaction diagrams, and its impact are shown by the dnorm "normalized contact distance", di "distance to the nearest nucleus internal to the surface", de "distance from the point to the nearest nucleus external to the surface", shape index "si", and curvedness "crv" as well as fragment batch "fb".

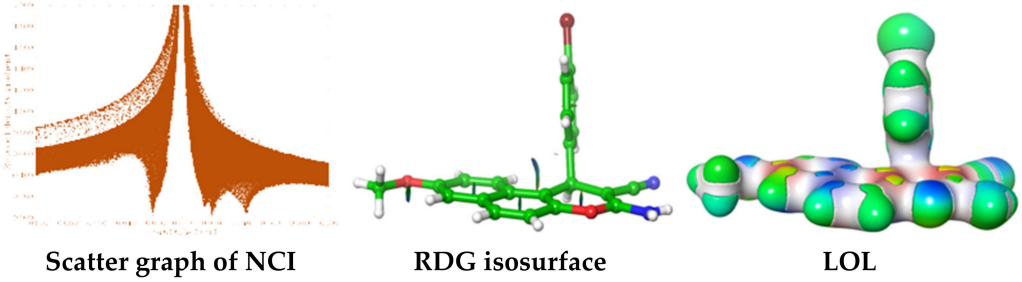

Figure 4. Different types of the weak interactions for compound **4**.

3.5. Theoretical Analysis for Molecule ***4***

DFT with B3LYP using 6-311**G(d,p) calculation in the gas phase was performed to correlate the experimental and theoretical findings. The results in Figure 5 showed a strong theoretical and experimental relation. The slight deviations between DFT and the experimental data because of the molecular interactions not being taken into account in the gas phase DFT simulation. The excellent correlation-coefficient (0.99) for bond length and angle revealed good agreement between the optimized geometry of the XRD and DFT data (Figure 5). These results confirm that the DFT optimized structure was close to that extracted in the experimental XRD analysis. Thus, in light of the DFT results, the electrical characteristics of compound **4** can be explored.

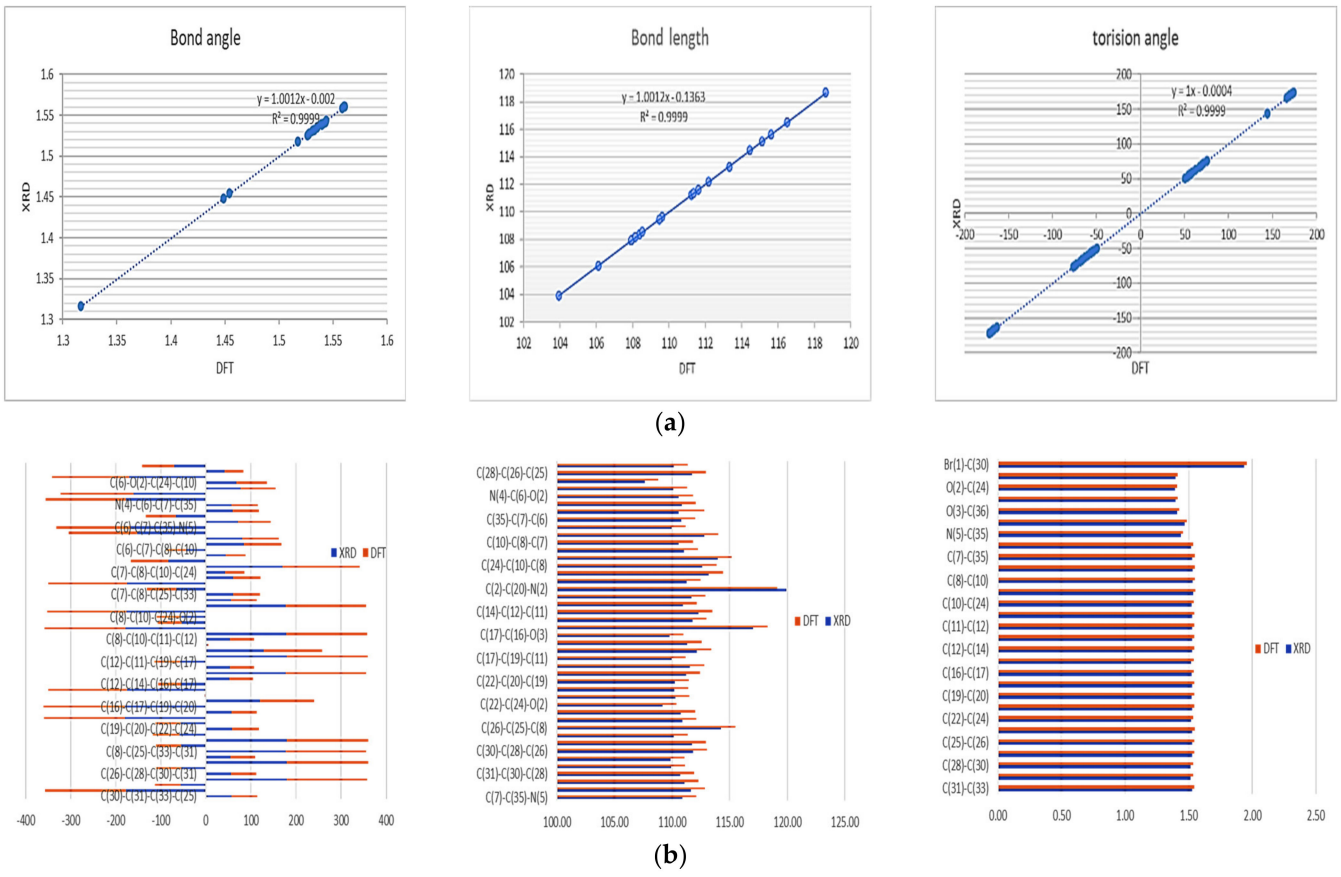

Figure 5. (**a**) The experimental XRD and DFT parameters. (**b**) Straight−line correlation for the geometric optimization parameters between the experimental and theoretical data.

TD-DFT for the molecules was performed to check their IR and UV–Visible absorption spectra and the findings are shown in Supplementary Materials Figures S4 and S5. The TD-DFT was performed on the optimized structure at the same basis set (B3LYP/6-311**G(d,p)

and the solvent effect was taken in consideration using the CPCM model and DMSO as the solvent. It was obvious from the TD-DFT measurements that the calculated absorption spectra showed bands in the range of 324–390 nm and 303–323 nm, respectively, which could be due to the intramolecular charge transfer from the donor (amino group) to the acceptor (cyano group). From the results, it is obvious that the intramolecular charge transfer (ICT) of compound **4** was bathochromically shifted.

The major goal of this part was to examine the "GR, global reactivity" of compound **4**, which was elucidated based on the "FMO, Fermi molecular orbital". Bultinck et al. [34] hypothesized that "one of the most used quantum chemical descriptors is the highest-energy-occupation for the molecular orbital (HOMO energy, donate area) and the lowest-unoccupied-energy for the molecular orbital (LUMO energy, acceptor area)". Figure 6 shows that HOMO was shifted over the whole benzopyran ring while LUMO was localized over the naphthalene ring. This means that intramolecular electron transfer over benzopyran takes place.

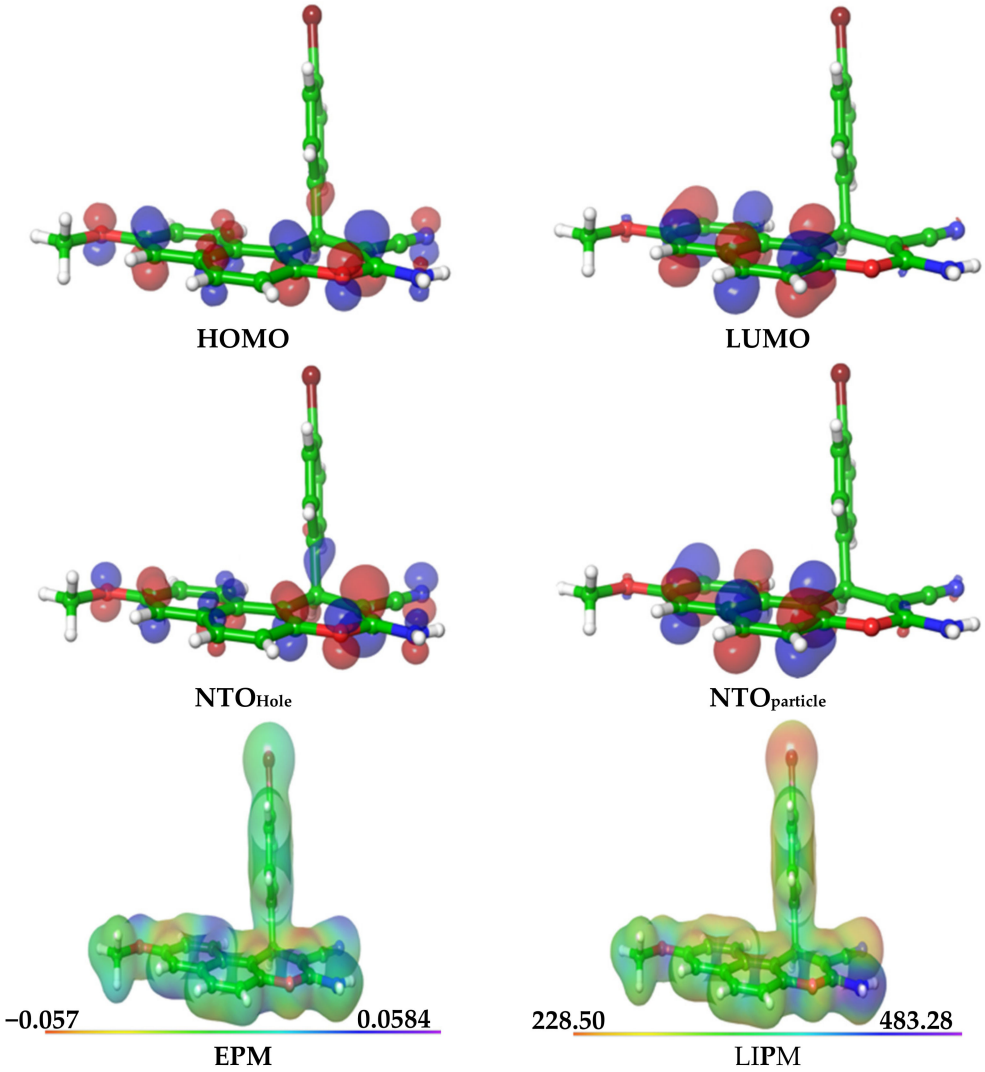

Figure 6. FMO of molecule **4** includes HOMO, LUMO, EPM, and LIPM.

The different parameters of GR were calculated as follows: "η, hardness"; "S, softness"; "χ, electronegativity"; "ω, electrophilicity index"; "εI, nucleophilicity index"; "I, ionization potential"; "A, electron affinity"; "ΔE_{B-D}, energy back donation"; "ΔN_{max}, maximum amount of electron transfer". The low "Δ_G, energy gap" reflects the high stability with the reactivity index.

The slight Δ_G = 0.16 a.u. was proportional to the soft molecule S = 12.75 a.u. Thus, compound **4** can be classified as a soft molecule combined with low kinetic stability. From Table 3, we noted a decrease in the εI, and ωi values, which increased their ability to attack against the biological receptors. The small $\Delta E_{B-D} = -0.026$ value refers to the low electron density, which transferred from the examined compound **4** to the biological system. $\Delta N_{max} = -0.605$ a.u. shows the high interaction ability with the biological system.

Table 3. The calculated GR for compound 4 using DFT/B3LYP/6-311**G(d,p).

HOMO	LUMO	Δ_G	η	S	χ	ωi	εI	I	A	ΔE_{B-D}	ΔN_{max}
−0.28	−0.04	0.16	0.07	12.75	−0.12	0.09	0.86	0.28	0.04	−0.026	−0.605
$= 1/2\left[\partial\, \mathbf{E}/\partial\, \mathbf{N^2}\right]_{v(r)}$		$\mathbf{S} = 1/\eta$		$\chi = -[\partial \mathbf{E}/\partial \mathbf{N}]_{v(r)}$		$\omega i = \mu^2/2\acute{\eta}$		$\varepsilon I = 1/\omega i$		$\Delta E_{B-D} = -\eta/4$	

The "NTOs, natural transition orbitals" pair provided evidence of the significance of the excitation state in the biological medium. We compared the NTO formalisms to the conventional canonical molecular orbital. NTOs provide further clarity into the responsibility of orbitals for the receptor's binding (Figure 6). From Figure 6, we can infer that the whole molecular skeleton of compound **4** can experience intramolecular charge transfer.

The "EPM, electrostatic potential map" and "LIPM, local ionization potential map" are depicted to determine how sensitive the molecular sites are to attacks from electrophiles and nucleophiles [35]. EPM was examined by the distribution of the electronic cloud around the reactive site, and computed the interaction and physiochemical features. The intermediate potential is represented by green-sites. The distribution and variation in colors over all four molecular skeletons were related to the difference in electrostatic potential. Figure 6 shows an increase in the green zone due to its high hydrophobicity, which is distinguished as the hydrophilicity area for the receptor.

LIPM is preferable to EPM [36] as its map designated site has electrons that are tightly bound and hence more slightly detached, and can be calculated by the Sjoberg equation [36]. The blue tint of the LIPM denotes the low electron density distribution around the molecular skeleton. Thus, the NH_2, OCH_3, and CN groups of molecule **4** are desirable sites for electrophilic attacks.

3.6. Antitumor Assay

A preliminary evaluation of the studied molecule **4** anti-tumor effectiveness against "MCF-7, breast cancer", "Adriamycin (ADR)-resistant human breast cancer, MCF-7/ADR" and two normal cell lines, "HFL-1, human fetal lung", "WI-38, human diploid fibroblasts" using the "MTT, 3-(4,5-dimethylthiazol-2-yl)-2,5-diphenyl tetrazolium bromide" colorimetric assay [37]. The in vitro cytotoxicity evaluation was achieved under different concentrations (0–100 μM). Doxorubicin and vinblastine were included in the experiments as a reference cytotoxic compound for the tested cell lines. The values for the growth inhibitory concentration (IC_{50} μM) were used to express the results, where the necessitated concentration produced a 50% inhibition of cell growth after 24 h of incubation, weighed against the untreated cell control (Table 4).

Compound **4** possessed high anti-proliferative activity against the MCF-7 cell line with IC_{50} 4.9 ± 0.25 μM compared with vinblastine (IC_{50} = 7.5 ± 0.03 μM) and exhibited moderate activity against doxorubicin (IC_{50} = 0.8 ± 0.0 μM), while compound **4** had excellent growth inhibitory activity against MCF-7/ADR with IC_{50} 13.6 ± 0.1 μM compared with doxorubicin (IC_{50} = 18.6 ± 0.2 μM).

Furthermore, compound **4** had inhibitory growth against HFL-1 and WI-38 with IC_{50} of 42.1 ± 0.2 μM and 51.7 ± 1.1 μM and there was limited activity against the control cell lines.

Table 4. Cytotoxic activity of the target compounds in the tested cell lines.

	IC_{50} μM [a]			
	Cancerotoxicity		**Normotoxicity**	
Compound	**MCF-7** [b]	**MCF-7/ADR**	**HFL-1**	**WI-38**
4	4.9 ± 0.25	13.6 ± 0.1	42.1 ± 0.2	51.7 ± 1.1
Vinblastine	7.5 ± 0.03			
Doxorubicin	0.8 ± 0.01	18.6 ± 0.2		

[a] The mean values of triplicate wells from at least three experiments, given in terms of the IC_{50} values with the mean and standard deviation; [b] IC_{50} = 2.5 ± 0.14 μg/mL [7].

3.7. Molecular Docking Simulations

In silico study was conducted to scrutinize the biological finding by using docking experiments against the wild-type EGFR-TKD (PDB ID: 1M17 [38] and PDB ID:4HJO [39]) and used the co-crystal erlotinib (AQ44) as the reference inhibitor, as shown in Figure 7. The designed molecule **4** exhibited superior docking scores and orientations compared to erlotinib (Table 5). The binding site for both proteins was the same, which included "GLN767, MET769, THR830, and ASP831" for both proteins [38,39]. The docking experiment was accomplished by Glide's module®. To validate the docking protocol, the original inhibitor [erlotinib "AQ44"] was redocked into the crystal structures of EGFR. The binding free energy Δ_G is listed in Table 5. The original inhibitor was suitably fitted into their own binding sites for their crystal structures. The most potent pose selected was based on the lowest Δ_G and rmsd.

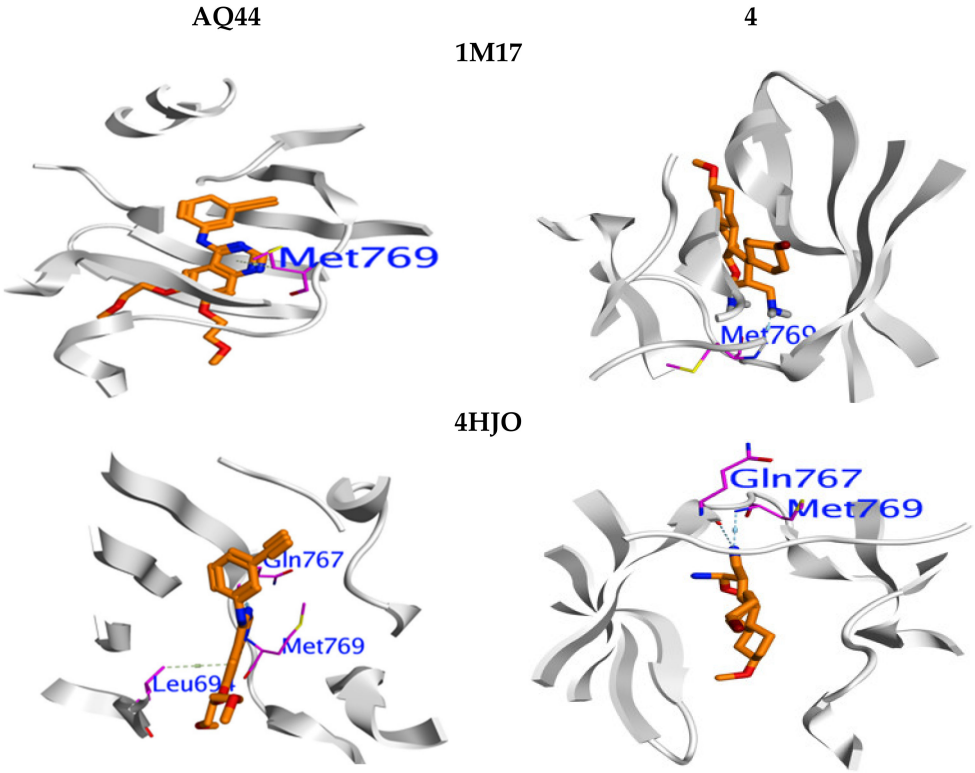

Figure 7. Binding manner for compound 4 over 1M17 and 4HJO compared to co-crystal erlotinib (AQ44) as the reference inhibitor.

Table 5. Docking score in (kcal/mol) for compound **4** against EGFR.

	ΔE	rmsd	H.B	EInt.	E_ele	Binding Region	Interaction	Distance
				1M17				
4	−6.43	1.73	−7.41	−29.95	−11.01	Met769	H-acceptor	2.49°
AQ44	−5.37	1.24	−8.17	−17.97	−9.20	Met769	H-donor	2.27°
				4HJO				
4	−8.86	1.46	−30.25	−25.94	−9.81	GLN767	H-donor	2.29°
						Met769	H-acceptor	2.27°
AQ44	−7.49	1.97	−25.27	−18.60	−9.29	GLN767	H-donor	2.23°
						Met769	H-acceptor	2.73°
						Leu694	pi-H	4.29

ΔE: Free binding energy of the ligand, EInt.: Binding affinity of H-bond interaction with receptor, H.B.: H-bonding energy between protein and ligand; Eele.: Electrostatic interaction over the receptor.

3.7.1. In the 1M17 Case

AQ44 was interacted with the vital MET 769 amino acid at a distance of 2.70 Å with H-interaction energy = −0.8 (kcal/mol). The investigated compound **4** was interacted with the same binding manner and formed a H-bond between the NH_2 group and (COOH) of Meth 769 with a distance of 2.49 Å with ΔE = −0.6 (kcal/mol). Furthermore, the free binding energy was predicted to further investigation of our biological finding. Compound **4** displayed a higher total binding affinity ΔE = −6.43 kcal/mol than AQ44 ΔE = −5.37 kcal/mol, which explains the promising potency (IC_{50} = 4.9 μM). Based on the results in Table 5, the H.B. interaction for molecule 4 (H.B. = −7.41 Kcal/mol) is the vital factor in the interaction. Furthermore, the energy framework (E_ele. = −11.1 Kcal/mol) showed that the interaction between compound 4 and the other residues was mainly contributed by the dispersion interaction.

3.7.2. In the 4HJO Case

Compound 4 had a higher binding score (ΔE =−8.86 kcal/mol) than AQ44 (ΔE =−8.86 kcal/mol) against 4HJO (Table 5). Compound 4 and the original inhibitor resisted 4HJO through forming the same important H-bonds with Met769 and Gln769 (Figure 7). Furthermore, AQ44 formed Π–Π interactions with Leu 694. These data explain the strong stability at active sites for the studied compound **4**.

Based on the energy framework analysis, the term E_int. is the most important contributor to ΔE, although the central molecule forms hydrogen bonds with its neighboring backbone residue.

3.8. Molecular Dynamic Simulations of Compound ***4***

The variation and stability of compound **4**, the C-alpha atoms-RMSD (root means square deviation) were analyzed. Figure 8 shows that the initial upper phase caused flexible behavior for their complexes. Furthermore, the complexes reached a steady state after 5 ns and maintained stability up to 41 and 61 ns for 4HJO, then stable until 100 ns, while in 1M17, the study state changed at 31 ns and the stability was maintained until the end of the segment.

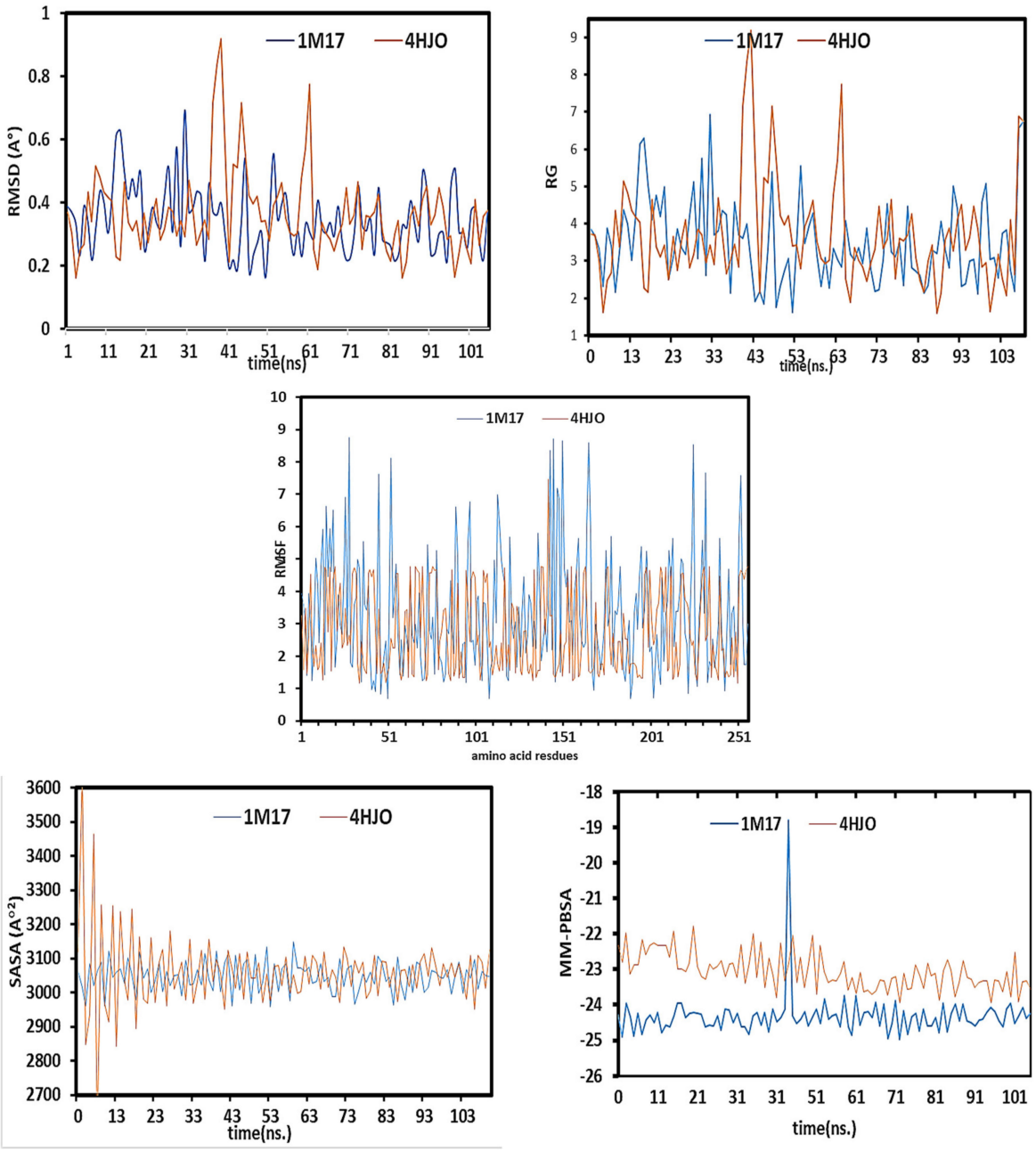

Figure 8. The molecular dynamic simulation for compound **4** at 100−ns simulation time.

As a result, the studied complexes had a RMSD less than 2.5 during the simulation, defining the complexes' stable comparative nature. The analyzed "RG, radius-gyration" along the studied trajectories showed the flexibility and mobility degree for the 1M17 and 4HJO complexes. The RG steady degree for the studied complexes appeared at 33 ns and 43 ns for 1M17 and 4HJO, respectively. The "RMSF, root-means-square-fluctuations" were also explored to investigate the flexibility of the residues of amino acids (Figure 9). The low RMSF <2.5 Å for 1M17 and 4HJO showed a high rigid degree for their complexes, while the increasing RMSF <6 Å for the BF-3 complex showed the relative flexibility degree of the backbone of the amino acid residues.

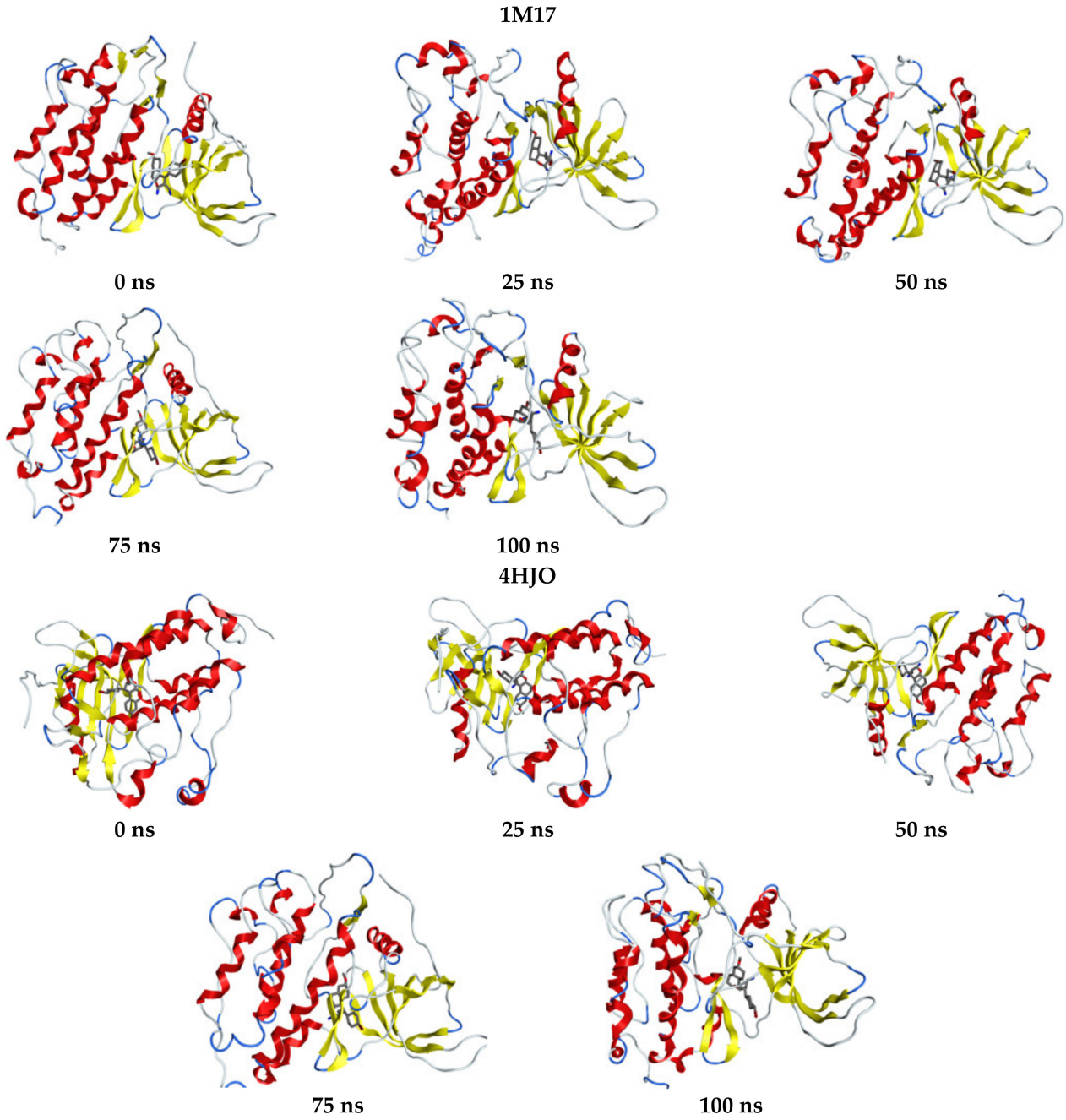

Figure 9. Snapshots of compound 4 with the 1M17 and 4HJO enzymes at different nanoseconds.

The "solvent-accessible-surface-area, SASA" simulation was studied for the investigated complexes to study the variation in the topology of the complexes, where the higher SASA learns the extent of the surface volumes. Lower SASA is defined by the elongated nature (Figure 9). The steady-state for 1M17 and 4HJO after 13 ns and the low variation degree for the SASA profiles along the simulation trajectories demonstrated their stable nature. Furthermore, all complexes had nearly the same SASA degree and described the condensed form of these protein complexes during the interaction of compound 4. Furthermore, the slight deviation for MM-PBSA for the overall time-scale, showed the strong interaction between the ligand and amino acid backbone for proteins, which showed a firm H-bonding pattern. The system behavior can be explained by the regularly changed binding pose of the compound at the binding pocket of the enzyme, where the binding affinity was stronger and still produced good intermolecular interactions. The different snapshot of compound 4 with the enzyme is given in Figure 9.

4. Conclusions

In conclusion, the microwave irradiation condition was used for the synthesis of the reported compound **4**, which was obtained in a crystal form and then characterized by single-molecule X-ray diffraction analysis. The DFT analysis was performed to study the intrinsic electronic properties of compound 4. Furthermore, to investigate intra- or intermolecular hydrogen bonding in our system, the DFT chemical reactivity, Hirshfeld and QTAIM tools were used, which showed that the $\pi\cdots\pi$ stacking interaction does not play an important role in the crystal packing. Molecule **4** was screened for its in vitro anti-proliferative ability against MCF-7, MCF-7/ADR, HFL-1, and WI-38 and divulged a high healthy selective cytotoxic proficiency against the malignant-cell lines, while it had no discernible effects on the normal cell lines. The EPM of compound 4 showed that the NH_2 fragment was the most negative site, which is responsible for the recognition of active amino acids in the receptor. The molecular docking showed that the most negative site was (NH_2), which involved its binding concerning the EGFR-TKD. This can be rationalized by the fact that the electrostatic interaction is not a principle factor in the interaction between (**4**) and the receptor. We considered ΔE and H.B. interactions as the principal interaction factors. In agreement with the results of the free energy calculation, the energy framework showed that the interaction between compound (**4**) and the receptor was mainly contributed by the dispersion interaction.

Supplementary Materials: The following supporting information can be downloaded at: https://www.mdpi.com/article/10.3390/cryst13010024/s1, Figure S1: ^{1}HNMR 8–6 ppm of compound **4**; Figure S2: ^{1}HNMR 10–0 ppm of compound **4**; Figure S3: ^{13}CNMR of compound **4**, the straight line correlation for geometric optimization parameters between experimental and theoretical data of compound **4**; Table S1: X-Ray data for investigated compounds **4**; Table S2: The experimental XRD and DFT parameters for compound **4**.

Author Contributions: M.H.A., A.M.F., A.E.-G.E.A., A.M.E.-A., L.M.A.-H. and R.M.O. designed the proposed methods and analyzed the spectral data; A.M.E.-A. performed the experiments and implemented the biological study; A.A.E. performed the docking study; H.A.G. and R.M.O. carried out and wrote the X-ray processes. All authors have read and agreed to the published version of the manuscript.

Funding: This work was funded by the Deanship of Science Research at King Khalid University, Saudi Arabia, who funded this work through the General Research Project under grant number (RGP.1/245/43).

Data Availability Statement: Not applicable.

Acknowledgments: The authors extend their appreciation to the Deanship of Science Research at King Khalid University, Saudi Arabia for funding this work through the General Research Project under grant number (RGP.1/245/43).

Conflicts of Interest: The authors declare no conflict of interest.

References

1. Pratap, R.; Ram, V.J. Natural and Synthetic Chromenes, Fused Chromenes, and Versatility of Dihydrobenzo[h]chromenes in Organic Synthesis. *Chem. Rev.* **2014**, *114*, 10476–10526. [CrossRef] [PubMed]
2. Killander, D.; Sterner, O. Synthesis of the bioactive benzochromenes pulchrol and pulchral, metabolites of Bourreria pulchra. *Eur. J. Org. Chem.* **2014**, *8*, 1594–1596. [CrossRef]
3. Singh, G.; Sharma, A.; Kaur, H.; Ishar, M. Chromanyl-isoxazolidines as Antibacterial agents: Synthesis, biological evaluation, quantitative structure activity relationship, and molecular docking studies. *Chem. Biol. Drug. Des.* **2016**, *87*, 213–223. [CrossRef] [PubMed]
4. Bingi, C.; Emmadi, N.R.; Chennapuram, M.; Poornachandra, Y.; Kumar, C.G.; Nanubolu, J.B.; Atmakur, K. One-pot catalyst free synthesis of novel kojic acid tagged 2-aryl/alkyl substituted-4H-chromenes and evaluation of their antimicrobial and anti-biofilm activities. *Bioorg. Med. Chem. Lett.* **2015**, *25*, 1915–1919. [CrossRef] [PubMed]
5. Vosooghi, M.; Rajabalian, S.; Sorkhi, M.; Badinloo, M.; Nakhjiri, M.; Negahbani, A.S.; Asadipour, A.; Mahdavi, M.; Shafiee, A.; Foroumadi, A. Synthesis and cytotoxic activity of some 2-amino-4-aryl-3-cyano-7-(dimethylamino)-4H-chromenes. *RPS* **2010**, *5*, 13–18.

6. Kasibhatla, S.; Gourdeau, H.; Meerovitch, K.; Drewe, J.; Reddy, S.; Qiu, L.; Zhang, H.; Bergeron, F.; Bouffard, D.; Yang, Q.; et al. Discovery and mechanism of action of a novel series of apoptosis inducers with potential vascular targeting activity. *Mol. Cancer Ther.* **2004**, *3*, 1365–1373. [CrossRef]
7. Ahmed, H.E.A.; El-Nassag, M.A.A.; Hassan, A.; Okasha, R.M.; Ihmaid, S.; Fouda, A.M.; Afifi, T.H.; Aljuhani, A.; El-Agrody, A.M. Introducing novel potent anticancer agents of 1H-benzo[f]chromene scaffolds, targeting c-Src kinase enzyme with MDA-MB-231 cell line anti-invasion effect. *J. Enzym. Inhib. Med. Chem.* **2018**, *33*, 1074–1088. [CrossRef]
8. Alblewi, F.F.; Okasha, R.M.; Eskandrani, A.A.; Afifi, T.H.; Mohamed, H.M.; Halawa, A.H.; Fouda, A.M.; Al-Dies, A.-A.M.; Mora, A.; El-Agrody, A.M. Design and synthesis of novel heterocyclic-based 4H-benzo[h]chromene moieties: Targeting antitumor caspase 3/7 activities and cell cycle analysis. *Molecules* **2019**, *24*, 1060. [CrossRef]
9. Alblewi, F.F.; Okasha, R.M.; Hritani, Z.M.; Mohamed, H.M.; El-Nassag, M.A.A.; Halawa, A.H.; Mora, A.; Fouda, A.M.; Assirid, M.A.; Al-Dies, A.M.; et al. Antiproliferative effect, cell cycle arrest and apoptosis generation of novel synthesized anticancer heterocyclic derivatives based 4H-benzo[h]chromene. *Bioorg. Chem.* **2019**, *87*, 560–571. [CrossRef]
10. El-Mawgoud, H.K.A.; Fouda, A.M.; El-Nassag, M.A.A.; Elhenawy, A.A.; Alshahrani, M.Y.; El-Agrody, A.M. Discovery of novel rigid analogs of 2-naphthol with potent anticancer activity through multi-target topoisomerase I & II and tyrosine kinase receptor EGFR & VEGFR-2 inhibition mechanism. *Chem. Biol. Interact.* **2022**, *355*, 109838.
11. El Gaafary, M.; Lehner, J.; Fouda, A.M.; Hamed, A.; Ulrich, J.; Simmet, T.; Syrovets, T.; El-Agrody, A.M. Synthesis and evaluation of antitumor activity of 9-methoxy-1H-benzo[f]chromene derivatives. *Bioorg. Chem.* **2021**, *116*, 105402. [CrossRef] [PubMed]
12. El-Agrody, A.M.; Fouda, A.M.; Assiri, M.A.; Mora, A.; Ali, T.E.; Alam, M.M.; Alfaifi, M.Y. In vitro anticancer activity of py-rano[3,2-c]chromene derivatives with both cell cycle arrest and apoptosis induction. *Med. Chem. Res.* **2020**, *29*, 617–629. [CrossRef]
13. Ahagha, M.H.; Dehghana, G.; Mehdipoura, M.; Teimuri-Mofradb, R.; Payamib, E.; Sheibanic, N.; Ghaffaria, M.; Asadi, M. Synthesis, characterization, anti-proliferative properties and DNA binding of benzochromene derivatives: Increased Bax/Bcl-2 ratio and caspase dependent apoptosis in colorectal cancer cell line. *Bioorg. Chem.* **2019**, *93*, 103329. [CrossRef] [PubMed]
14. Dgachi, Y.; Bautista-Aguilera, O.M.; Benchekroun, M.; Martin, H.; Bonet, A.; Knez, D.; Godyn, J.; Malawska, B.; Gobec, S.; Chioua, M.; et al. Synthesis and biological evaluation of benzochromenopyrimidinones as cholinesterase inhibitors and potent antioxidant, non-hepatotoxic agents for Alzheimer's disease. *Molecules* **2016**, *21*, 634. [CrossRef] [PubMed]
15. Cravotto, G.; Carnaroglio, D. *Microwave Chemistry*; De Gruyter: Berlin, Germany; Boston, MA, USA, 2017; p. 9873110479928.
16. Amariucai-Mantu, D.; Mangalagiu, V.; Danac, R.; Mangalagiu, I.I. Microwave assisted reactions of Azahetero-cycles formedic-inal chemistry applications. *Molecules* **2020**, *25*, 716. [CrossRef]
17. Ahmed, M.N.; Ghias, M.; Shah, S.W.A.; Shoaib, M.; Tahir, M.N.; Ashfaq, M.; Ibrahim, M.A.A.; Andleeb, H.; Gilf, D.M.; Frontera, A. X-ray characterization, Hirshfeld surface analysis, DFT calculations, in vitro and in silico lipoxygenase inhibition (LOX) studies of dichlorophenyl substituted 3-hydroxychromenones. *New J. Chem.* **2021**, *45*, 19928–19940. [CrossRef]
18. Sheldrick, G.M. A short history of SHELX. *Acta Crystallogr.* **2008**, *64*, 112–122. [CrossRef]
19. Sheldrick, G.M. SHELXTL-PC. version 5.1. Siemens Analytical Instruments, Inc.: Madison, WI, USA, 1997.
20. Schrödinger, M. *Schrödinger, Schrödinger Release 2018-1*; Schrödinger: New York, NY, USA, 2018.
21. Lu, Y.; Zhang, B.; Wang, N.; Li, M.; Xi, N. Investigation of Major Flavonoids from Artemisia argyi as a Potential COVID-19 Drug: Molecular Docking and DFT Calculations. *Crystals* **2022**, *12*, 990. [CrossRef]
22. El Gaafary, M.; Syrovets, T.; Mohamed, H.M.; Elhenawy, A.A.; El-Agrody, A.M.; El-Galil, E.; Amr, A.; Ghabbour, H.A.; Almehizia, A.A. Synthesis, Cytotoxic Activity, Crystal Structure, DFT Studies and Molecular Docking of 3-Amino-1-(2, 5-dichlorophenyl)-8-methoxy-1 H-benzo [f] chromene-2-carbonitrile. *Crystals* **2021**, *11*, 184. [CrossRef]
23. Lu, X. DC-CFractal Geometry and Architecture Design: Case Study Review. *Chaotic Model. Simul.* **2012**, *311*, 322.
24. Zhang, Y.; Zhang, T.J.; Tu, S.; Zhang, Z.H.; Meng, F.H. Identification of novel Src inhibitors: Pharmacophore-based virtual screening, molecular docking and molecular dynamics simulations. *Molecules* **2020**, *25*, 4094. [CrossRef] [PubMed]
25. Ouassaf, M.; Belaidi, S.; Chtita, S.; Lanez, T.; Abul Qais, F.; Md Amiruddin, H. Combined molecular docking and dynamics simulations studies of natural compounds as potent inhibitors against SARS-CoV-2 main protease. *J. Biomol. Struct. Dyn.* **2021**, *27*, 1–10. [CrossRef] [PubMed]
26. Belhassan, A.; Zaki, H.; Chtita, S.; Alaqarbeh, M.; Alsakhen, N.; Benlyas, M.; Lakhlifi, T.; Bouachrine, M. Camphor, Artemisinin and Sumac Phytochemicals as inhibitors against COVID-19: Computational approach. *Comput. Biol. Med.* **2021**, *136*, 104758. [CrossRef] [PubMed]
27. Hasan, A.H.; Murugesan, S.; Amran, S.I.; Chander, S.; Alanazi, M.M.; Hadda, T.B.; Shakya, S.; Pratama, M.R.F.; Das, B.; Biswas, S.; et al. Novel thiophene Chalcones-Coumarin as acetylcholinesterase inhibitors: Design, synthesis, biological evaluation, molecular docking, ADMET prediction and molecular dynamics simulation. *Bioorganic Chem.* **2022**, *119*, 105572. [CrossRef] [PubMed]
28. Alhomrani, M.; Alsanie, W.F.; Alamri, A.S.; Alyami, H.; Habeeballah, H.; Alkhatabi, H.A.; Felimban, R.I.; Haynes, J.M.; Shakya, S.; Raafat, B.M.; et al. Enhancing the Antipsychotic Effect of Risperidone by Increasing Its Binding Affinity to Serotonin Receptor via Picric Acid: A Molecular Dynamics Simulation. *Pharmaceuticals* **2022**, *15*, 285. [CrossRef]
29. Replace 29 by Allen, F.H.; Kennard, O.; Watson, D.G.; Brammer, L.; Orpen, A.G.; Taylor, R. Tables of Bond Lengths determined by X-Ray and Neutron Diffraction Part. *J. Chem. Soc. Perkins Trans.* **1987**, *2*, 1–19. [CrossRef]

30. Mackenzie, C.F.; Spackman, P.R.; Jayatilaka, D.; Spackman, M.A. Crystal Explorer model energies and energy frameworks: Extension to metal coordination compounds, organic salts, solvates and open-shell systems. *IUCrJ* **2017**, *4*, 575–587. [CrossRef]
31. Henkelman, G.; Arnaldsson, A.; Jonsson, H. A fast robust algorithm Bader decomposition of charge density. *Comput. Master. Sci.* **2003**, *36*, 354–360. [CrossRef]
32. Akman, F.; Issaoui, N.; Kazachenko, A.S. Intermolecular hydrogen bond interactions in the thiourea/water complexes (Thio-(H2O) n)(n = 1, . . . , 5): X-ray, DFT, NBO, AIM, and RDG analyses. *J. Mol. Model* **2020**, *26*, 161. [CrossRef]
33. Zhou, X.-Y.; Rong, C.; Lu, T.; Zhou, P.; Liu, S. Information functional theory: Electronic properties as functionals of information for atoms and molecules. *J. Phys. Chem.* **2016**, *120*, 3634–3642. [CrossRef]
34. Bultinck, P.; Winter, H.D.; Langenaeker, W.; Tollenare, J.P. *Computational Medicinal Chemistry for Drug Discovery*; CRC Press: Boca Raton, FL, USA, 2003.
35. Politzer, P.; Murray, J.S.; Bulat, F.A. Average local ionization energy: A review. *J. Mol. Model.* **2010**, *16*, 1731–1742. [CrossRef] [PubMed]
36. Sjoberg, P.; Murray, J.S.; Brinck, T.; Politzer, P. Average local ionization energies on the molecular surfaces of aromatic systems as guides to chemical reactivity. *Can. J. Chem.* **1990**, *68*, 1440–1443. [CrossRef]
37. Mosmann, T. Rapid colorimetric assay for cellular growth and survival: Application to proliferation and cytotoxicity assays. *J. Immunol. Methods* **1983**, *65*, 55–63. [CrossRef] [PubMed]
38. Stamos, J.; Sliwkowski, M.X.; Eigenbrot, C. Structure of the epidermal growth factor receptor kinase domain alone and in complex with a 4-anilinoquinazoline inhibitor. *J. Biol. Chem.* **2002**, *48*, 46265–46272. [CrossRef] [PubMed]
39. Park, J.H.; Liu, Y.; Lemmon, M.A.; Radhakrishnan, R. Erlotinib binds both inactive and active conformations of the EGFR tyrosine kinase domain. *Biochem. J.* **2012**, *448 Pt 3*, 417. [CrossRef]